Journal of Materials Chemistry C

PAPER

Check for updates

CuSCN as a hole transport layer in an inorganic solution-processed planar Sb₂S₃ solar cell, enabling carbon-based and semitransparent photovoltaics†

Pankaj Kumar, [iD] [a] Shujie You[a] and Alberto Vomiero*[ab]

Sb₂S₃ is an emerging inorganic photovoltaic absorber material with attractive properties such as high absorption coefficient, stability, earth-abundance, non-toxicity, and low-temperature solution processability. Furthermore, with a bandgap of *ca.* 1.7 eV, it can also be used in semitransparent or tandem solar cell applications. Here, an inorganic wide-bandgap hole transport layer (HTL), copper thiocyanate (CuSCN), is used in an Sb₂S₃ solar cell employing a simple planar geometry. The compact and highly transparent CuSCN HTL was compatible with the low-cost, blade-coated carbon/Ag electrode and a semitransparent solar cell device. With Au and carbon/Ag electrodes, chemical bath deposited Sb₂S₃ solar cells achieved power conversion efficiencies (PCEs) of 1.75% and 1.95%, respectively. At the same time, a preliminary semitransparent Sb₂S₃ device with an ultrathin Au (∼15 nm) electrode showed a good average visible transmittance (AVT) of 26.7% at a PCE of 1.65%.

Introduction

Photovoltaics technology has the potential to meet the increasing global demand for clean and sustainable renewable energy. Crystalline and poly-crystalline silicon (Si) solar cells have been successfully commercialized, while CIGS (Cu(In, Ga)(S, Se)₂), CdTe, perovskites, dye-sensitized solar cells, and organic solar cells have been commercialized only to some extent.[1–5] However, these technologies have challenges, such as using critical raw materials, toxicity, long-term instability, or limited application flexibility.[2,6–8] These limitations of relatively mature photovoltaic technologies have motivated researchers to search for new absorber materials that are more efficient, stable, green, and cheap.[9] These emerging inorganic absorbers include, for example, chalcogenides (sulfides, selenides, and tellurides), oxides, nitrides, phosphides, and halides (mainly bromides and iodides).[2] Among them, a binary semiconducting chalcogenide of the V₂–VI₃ family, antimony sulfide (Sb₂S₃), has attracted considerable attention in recent years for its high absorption coefficient (1.8 × 10⁵ cm⁻¹ at 450 nm), suitable optical bandgap (∼1.7 eV with a theoretical Shockley–Queisser limit of PCE = 28.64%),

long-term stability, elemental abundance, and low processing temperatures.[10–12] In addition, Sb₂S₃ has a unique quasi 1-D crystal structure (*Pnma* space group) which consists of covalently bonded [Sb₄S₆]ₙ ribbon units (along [001] or *c* direction) stacked together by weak van der Waals force in a perpendicular direction, forming layered sheets of Sb₂S₃. Charge transport along the ribbon is more efficient than charge hopping between ribbons. Also, these ribbons are free of dangling bonds and thus form benign grain boundaries, thus reducing bulk recombination if the growth direction is controlled in the [*hk*1] direction.[13–17]

Sb₂S₃ has been applied in either mesoporous (often called sensitized solar cells based on the existing dye-sensitized solar cell technology) or planar heterojunction configurations. The tuning of the morphology and crystallinity of the Sb₂S₃ absorber layer has resulted in high PCE in both planar and mesoporous devices.[11,16,18] In mesoporous Sb₂S₃ solar cells, a thin absorber layer (∼10 nm) is deposited on a nanocrystalline mesoporous TiO₂ scaffold, and the pores are then filled with a hole transport material (HTM). In this design, fast carrier transfer and enhanced absorption result in high current densities, but the open-circuit voltages (V_{OC}) suffer because of increased carrier recombination.[19] This limitation can be circumvented in planar solar cells with a compact Sb₂S₃ absorber layer, thus potentially achieving a higher V_{OC}.[20] Boix *et al.*[21] compared flat and nanostructured TiO₂/Sb₂S₃/P3HT devices (P3HT stands for poly(3-hexylthiophene)). Although the nanostructured cell showed higher performance than the flat cell due to higher short circuit current density (J_{SC}) and fill factor (FF), V_{OC} was higher for

a Division of Materials Science, Department of Engineering Sciences and Mathematics, Luleå University of Technology, SE-971 87, Luleå, Sweden.
E-mail: Alberto.vomiero@ltu.se
b Department of Molecular Sciences and Nanosystems, Ca' Foscari University of Venice, Via Torino 155, 30172, Venezia Mestre, Italy
† Electronic supplementary information (ESI) available. See DOI: https://doi.org/10.1039/d2tc03420d

the flat device (0.56 vs. 0.48 V). Additionally, due to reproducible and scalable device fabrication with fewer processing steps, a planar device structure is preferable. However, the efficiencies of mesoporous devices are still superior—the highest PCEs for planar and mesoporous Sb_2S_3 solar cells stand at 7.10% (V_{OC}: 0.72 V, J_{SC}: 17.24 mA cm^{-2}, and FF: 0.57)[22] and 7.5% (V_{OC}: 0.71 V, J_{SC}: 16.1 mA cm^{-2}, and FF: 0.65),[23] respectively. Nevertheless, planar solar cells have several other comparative advantages that make them more attractive—realization of semitransparent photovoltaics, simpler and scalable fabrication, and flexible substrate compatibility.[24–28]

Several organic and inorganic hole transport layers (HTLs) have been applied in Sb_2S_3 absorber based solar cells, including 2,2′,7,7′-tetrakis(*N,N*-di-*p*-methoxyphenylamine)-9,9′-spirofluorene (Spiro-OMeTAD), poly(2,6-(4,4-bis-(2 ethylhexyl)-4*H*-cyclopenta[2,1-*b*;3,4-*b*′]dithiophene)-*alt*-4,7(2,1,3-benzothiadiazole) PCPDTB, P3HT, copper thiocyanate (CuSCN), copper iodide (CuI), nickel oxide (NiO$_x$), and vanadium oxide (V$_2$O$_5$).[29–33] Organic HTLs suffer from inherent chemical and thermal instability. On the other hand, inorganic HTLs enhance the devices' stability. Among these inorganic HTLs, CuSCN is cheap, abundant, and thermally stable with high hole mobility and transparency. Specifically, CuSCN has optimal optoelectronic properties to act as an efficient HTL with a wide bandgap (E_g) of ~3.6 eV, a suitable mobility of 0.001–0.1 cm^2 V^{-1} s^{-1}, and appropriate energy levels (valence band, E_{VB} = −5.4 eV with respect to vacuum).[34,35] Additionally, in Sb_2Se_3 solar cells, Cu diffusion (from CuSCN) into the Sb_2Se_3 grain boundaries has been reported to passivate grain boundaries and reduce recombination.[36] A similar passivating effect can be expected since Sb_2S_3 has the same quasi-1-D crystal structure and similar physiochemical properties.[37] Cu doping was found to be beneficial for solar cell device performance.[38]

Fully inorganic solar cells based on Sb_2S_3 and CuSCN HTL have been reported by several groups, mainly for a sensitized architecture with a TiO$_2$ nanoporous layer as the ETL. Itzhaik *et al.*[39] reported a PCE of 3.37% in an Sb_2S_3-sensitized nanoporous solar cell architecture (FTO/compact or dense TiO$_2$-(c-TiO$_2$)/porous-TiO$_2$, (p-TiO$_2$)/In–OH–S/Sb_2S_3/KSCN treatment/CuSCN/Au). The Sb_2S_3 film was pretreated with 0.5 M aqueous KSCN solution before infiltration with a CuSCN solution to passivate the CuSCN/Sb_2S_3 interface or to dope the CuSCN layer. Tsujimoto *et al.*[40] fabricated Sb_2S_3 sensitized solar cells with KSCN treated-CuSCN as the HTL layer and achieved a PCE of 2.82% with a device structure of c-TiO$_2$/p-TiO$_2$/Sb_2S_3/CuSCN/Au, which was further improved to 4.1% via TiO$_2$ surface treatment. Subsequently, they doped Sb_2S_3 with Ti and achieved a PCE of 5.7%.[41]

On the other hand, for planar Sb_2S_3 solar cells with CuSCN as the HTL layer, the efficiencies have remained lower than those with organic HTLs.[28,33,42] Muto *et al.*[42] fabricated a planar Sb_2S_3 solar cell (FTO/c-TiO$_2$/Sb_2S_3/CuSCN/Au) and achieved a PCE of 0.8%, compared to nanoporous architecture with a nanocrystalline TiO$_2$ along with compact TiO$_2$ (FTO/c-TiO$_2$/nc-TiO$_2$/Sb_2S_3/CuSCN/Au) with a PCE of 3.6%. Mayon *et al.*[33] reported an inorganic planar Sb_2S_3 solar cell with an efficiency of 1.7% (highest PCE for a planar Sb_2S_3 solar cell with a CuSCN HTL) with evaporated Sb_2S_3 and 0.8% for solution deposited Sb_2S_3. Considering the advantages of the planar architecture and the improved stability of inorganic CuSCN as the HTL, more studies are needed for this device configuration to realize its full potential.

In recent years, there has been growing interest in semi-transparent photovoltaics (ST-PV) for building integrated applications (BIPVs).[43–48] Sb_2S_3 has a relatively wide bandgap and high absorption coefficient—promising attributes for ST-PV applications. Lee *et al.*[24] reported an atomic layer deposited (ALD)-Sb_2S_3 semitransparent solar cell (ITO/ALD-TiO$_2$/ALD-Sb_2S_3/P3HT/Au-10 nm) with a PCE of 3.44% and an average visible transmittance (AVT) of 13% resulting in a light utilization efficiency (LUE = PCE × AVT/100) of 0.45. Zhang *et al.*[27] achieved a PCE of 2.18% for a 100 nm hydrothermally deposited Sb_2S_3 solar cell with graphene as the top electrode (FTO/CdS/Sb_2S_3/Spiro-OMeTAD/graphene). The AVT value was not reported but can be calculated to be around 15% from the transmission curve of the device (LUE ≈ 0.33). Zimmermann *et al.*[28] and Eensalo *et al.*[25] have also reported ST-Sb_2S_3 solar cells with 100 nm and 70 nm Sb_2S_3 absorber layers, respectively, and P3HT as the HTL. However, the AVTs of the complete ST devices with electrodes were not reported. Overall, the PCEs of ST-Sb_2S_3 devices have remained relatively low because of the drastic drop in V_{OC} and FF for thinner absorber layers, along with a proportional decrease in J_{SC}.[27,49]

In most high-performance devices, gold as the counter electrode is ubiquitous.[20,22,50–52] However, the high cost (~100 USD m^{-2}) and the upscaling issue of vacuum deposition raise concerns about the large-scale commercialization of these solar cells.[53] Carbon (carbon black and graphite) is a cheaper alternative to metal-based electrodes. Carbon electrodes have high electrochemical stability and suitable work function, WF (−5.0 eV vs. −5.1 eV for Au) in combination with CuSCN with a suitably aligned VB of −5.4 eV.[54]

This work presents a fully inorganic planar Sb_2S_3 solar cell based on CuSCN as the HTL. At the same time, it is shown that a low-cost conductive carbon paste can replace the expensive gold top electrode in this device structure. With the optimized CuSCN film as the HTL, more than double the efficiency has been obtained compared to the previous highest performance reported by Mayon *et al.*[33] for a similar device structure (1.75% vs. 0.8%, respectively). The carbon top electrode further improved the PCE to 1.95%. Moreover, with this combination of non-toxic inorganic TiO$_2$ and CuSCN as the ETL and the HTL, respectively, a promising ST-Sb_2S_3 is demonstrated, achieving an AVT of 26.7% and a PCE of 1.65% (LUE = 0.45), at par with the highest reported LUE using an organic HTL layer (LUE = 0.45 was reported by Lee *et al.*[24] using organic P3HT as the HTL).

Experimental

Device fabrication

Patterned FTO substrates were cleaned using Hellmanex solution (3 vol% in water), distilled water, acetone, and isopropanol,

16274 | *J. Mater. Chem. C*, 2022, **10**, 16273–16282

This journal is © The Royal Society of Chemistry 2022

respectively, for 10 min each, followed by drying in an oven for 30 min at 120 °C. A compact TiO_2 layer was spin-coated on the cleaned FTO using the sol–gel method.[55] Briefly, titanium(IV) isopropoxide (369 μL) was diluted with 2.53 mL absolute ethanol. To this solution, a separate diluted HCL solution containing 35 μL HCL (2 M) in 2.53 mL absolute ethanol was added dropwise while maintaining vigorous magnetic stirring. Before spin coating, the resultant clear solution was filtered with a PTFE filter with a 0.45 μM pore size. To achieve an optimized thickness of ~60–70 nm, two spin coatings were done, at 2000 and 4000 rounds per minute (RPM), respectively. The coated films were dried at 200 °C for 10 minutes and then annealed at 500 °C for 60 minutes. Sb_2S_3 films were deposited using a conventional chemical bath deposition method.[32,56] 650 mg $SbCl_3$ was dissolved in 2.5 mL acetone, followed by the addition of 25 mL 1 M sodium thiosulphate and 72.5 mL deionized water. Film thickness was optimized by controlling the duration of CBD (~15–45 min at 7–10 °C) and the performance parameters of the devices with varying CBD times are shown in Fig. S1a and Table S1 (ESI†). The cross-section images of Sb_2S_3 for these CBD times are shown in Fig. S2 (ESI†). The film starts with island-type growth and progressively becomes less porous. The coated films were immediately rinsed in distilled water and dried using compressed air. The backsides of the substrates were cleaned with a dilute HCl solution. These shiny yellow films were annealed in an N_2 environment at an optimized temperature of 320 °C (optimization data are shown in Fig. S1b and Table S2, ESI†) on a hotplate for 10 min to improve the crystallinity. A dark brown stibnite phase was obtained (see Fig. S3a, b, and d, ESI†), following the previous reports.[28,32] CuSCN was spin-coated from a diethyl sulfide (DES) solution. Copper(I) thiocyanate powder (99% from Sigma-Aldrich) was dissolved in DES at a concentration of 35 mg mL^{-1} and stirred overnight at RT.[57] The optimized spinning speed was 4000 RPM, resulting in a thickness of ~60–70 nm. Devices with 2000 RPM (~110 nm) and 6000 RPM (~45 nm) had lower performances, shown in Fig. S1c and Table S3 (ESI†). The drying conditions were critical to obtaining a smooth reflective surface. After spin coating, the films were left to slow dry at room temperature for 30 minutes prior to a heat treatment at 90 °C for 10 minutes to remove the residual solvent. Immediate heat treatment resulted in a visibly rough surface, not suitable for ST devices and repeatability. A carbon top contact was formed using blade coating carbon (Agar Leit C carbon cement) of thickness ~30–50 μm, which was subsequently covered with Ag paste to decrease the contact resistivity. This blade-coated C/Ag electrode is called C-electrode for simplicity. For devices with an Au electrode (ca. 100 nm for an opaque device or ca. 15 nm for the ST device), a compact sputter coater (a Leica EM ACE 200, Leica Microsystems GmbH, Wetzlar, Germany) was used.

Characterization and measurements

The optical characterization studies (transmittance, absorbance, and reflectance) were performed using a Cary 5000 spectrophotometer equipped with an integrating sphere. The optical bandgap, E_g, of thin films, was extracted using Tauc's formula:

$(\alpha h\nu)^{\gamma} = C(h\nu - E_g)$, where α is the absorption coefficient, $h\nu$ is the photon energy, C is a constant, and γ takes the values of 2 or $\frac{1}{2}$ for direct and indirect bandgap, respectively.[58] The absorption coefficient, α, was calculated using the equation: $\alpha = A \ln 10/t$, where A is the absorbance and t is the thickness of the film determined by cross section SEM.[59] For Sb_2S_3 films, direct band gap fitting ($\gamma = 2$) agreed with the data well (with a good linear relationship between $(\alpha h\nu)^{\gamma}$ versus $h\nu$ plot), as reported elsewhere.[12,60,61] Similarly, direct bandgap was calculated for the CuSCN thin film based on previous reports.[62,63] AVT was calculated using the equation:

$$AVT = \frac{\int^{T}(\lambda) \cdot V(\lambda) \cdot AM1.5G(\lambda)d\lambda}{\int^{V}(\lambda) \cdot AM1.5G(\lambda)d\lambda}$$

where λ is the wavelength, $T(\lambda)$ is the transmission spectrum, $V(\lambda)$ is the photopic response of the human eye, and AM1.5G represents the solar photon flux.[64] The morphology and cross-section of films/devices were characterized by Magellan 400 Field Emission Scanning Electron Microscopy (FESEM). X-Ray diffraction patterns (XRD) were collected on a PANalytical Empyrean X-ray diffraction diffractometer with a Cu K_α source. Rutherford backscattering (RBS) was carried out using a 2.0 MeV $^4He^+$ beam in IBM geometry at normal incidence and a backscattering angle θ of 160°.

The current density–voltage (J–V) measurements were performed using a Keithley 2400 source meter under simulated AM 1.5G irradiation (100 mW cm^{-2}) with a standard 100 W Xe lamp-based solar simulator Oriel LCS-100 (default scan parameters: forward scan from −1 V to 1 V; scan rate: 100 mV s^{-1}). The illumination intensity was calibrated by a monocrystalline silicon reference cell (Oriel 91150) P/N). The measured pixel area of the device is 5–6 mm^2, defined using a black mask. The external quantum efficiency (EQE) was measured using the Rera SpeQuest quantum efficiency system. Electrochemical impedance spectroscopic (EIS) measurements were performed using an electrochemical workstation (Solartron Analytical, ModulabXM) in the frequency range from 1 MHz to 10 Hz with an applied potential of 0.5 V in the dark.[20] For Mott–Schottky analysis, the frequency was set at 10 kHz, and the measurements were performed in the dark. Circuit-based fitting was performed using an EIS Spectrum Analyzer developed by Bondarenko et al.[65]

A numerical simulation program, SCAPS-1D, developed by Burgelman et al.,[66] was used to calculate the band diagram of the device structure at the short circuit (applied bias = 0 V) to visualize the injection/extraction barriers at the Sb_2S_3/CuSCN interface. The simulated structure consists of FTO/TiO_2/Sb_2S_3/CuSCN with flat band contacts. The parameters and material properties are listed in Table S4 (ESI†), along with the corresponding references.

Results and discussion

Fig. 1a and b depict the energy levels of the device structure and the corresponding SCAPS-1D-modeled band diagram. CuSCN

This journal is © The Royal Society of Chemistry 2022

J. Mater. Chem. C, 2022, **10**, 16273–16282 | **16275**

layer functions as both electron blocking (because of its low conduction band energy level) and hole transport layers (because of its VB lying close to that of Sb_2S_3). The importance of appropriate processing of the CuSCN film to prepare a high-quality uniform film with optimum thickness has been described elsewhere.[57,67–71] Based on these reports, the CuSCN film preparation conditions (spin speed, concentration, and drying conditions) were optimized to obtain a smooth and transparent film with a wide bandgap of *ca.* 3.85 eV (Fig. S3a and c, ESI†), consistent with the values reported elsewhere.[54,72]

The absorption coefficient and photograph of a CuSCN film coated on glass are shown in Fig. 1c (in Fig. S3a, ESI,† the absorption coefficients of Sb_2S_3 and CuSCN are shown for comparison). The film appeared quite smooth after the optimized drying step. The XRD pattern of the CuSCN thin film and CuSCN powder (as received from Sigma-Aldrich) is shown in Fig. 1d. The peak located at $16.1°$ (003) is visible in ~ 60 nm thin CuSCN, suggesting a crystalline β-CuSCN phase (while the powder spectrum matches too with the JCPDS #29-0581 standard for β-CuSCN).[72]

The top surface SEM image of the spin-coated CuSCN film on Sb_2S_3 (Fig. 2d) showed a full coverage of the island-like Sb_2S_3 layer (Fig. 2c), which would act as a good recombination barrier.[33] The cross-section SEM images of the optimized Au- and C-electrode-based devices are shown in Fig. 2a and b, respectively, with an optimized CuSCN thickness of ~ 60–70 nm—an optimum balance between the lowest resistance and full coverage film as evidenced in the photovoltaic performances of lower and higher RPMs in Fig. S1c and Table S3 (ESI†).[73,74] Furthermore, to replace the vacuum-deposited Au electrode with a low-cost blade-coated carbon electrode, compatibility of the HTL with the solvent used in carbon paste was also verified. The CuSCN solid film was resistant to carbon paste solvent (mixture of acetone, 2-methoxy-1-methyl ethyl acetate, and xylene) as evident in the SEM image (Fig. S5a and b, ESI†) and absorption
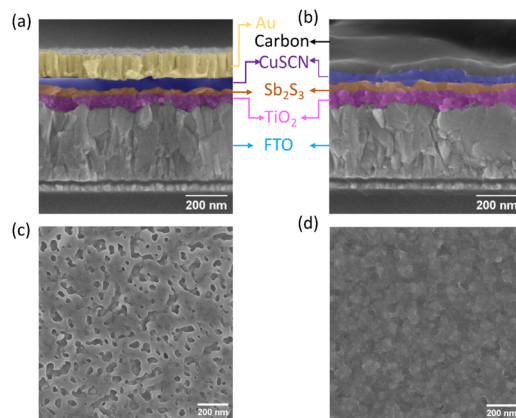

Fig. 2 Cross-section of Sb_2S_3 solar cells with CuSCN as the HTL with (a) an Au electrode and (b) a carbon electrode (a zoomed-out view is shown in Fig. S4, ESI†). SEM image of the top surface of (c) the annealed Sb_2S_3 film and (d) CuSCN deposited on top of the Sb_2S_3 film.

Table 1 Photovoltaic performance of ultrathin Sb_2S_3 planar solar cells with CuSCN as the HTL and varying electrodes

Top electrode		V_{OC} [V]	J_{SC} [mA cm^{-2}]	FF	PCE [%]
Au	Best device	0.501	7.10	0.50	1.75
	Average[a]	0.54 ± 0.02	6.75 ± 0.50	0.45 ± 0.03	1.64 ± 0.1
Carbon	Best device	0.611	6.25	0.51	1.95
	Average[a]	0.62 ± 0.02	5.91 ± 0.45	0.48 ± 0.03	1.76 ± 0.1

[a] Average and standard deviation from 15 devices.

spectrum (Fig. S5c, ESI†) of the CuSCN surface without and with solvent treatment.

Table 1 lists the photovoltaic performance of Sb_2S_3 solar cells based on sputtered gold (Au-electrode) and carbon/Ag-paste electrode (C-electrode), and the corresponding device structures are shown in Fig. 2a and b. Fig. 3a shows the current density–voltage (J–V) curves for the champion devices, and the corresponding statistical analysis is shown in Fig. S6 (ESI†). A PCE of 1.95% (V_{OC} = 0.611 V, J_{SC} = 6.25 mA cm^{-2}, and FF = 0.51) was obtained with a carbon electrode, while the device using the Au electrode exhibited a PCE of 1.75% with slightly improved J_{SC} (7.10 mA cm^{-2}) and lower V_{OC} (0.501 V) and a similar FF (0.50). These PCEs are better than those reported in the literature for solution-processed planar Sb_2S_3 solar cells using CuSCN as the HTL with considerably improved V_{OC} (see Table S5, ESI† for comparison with previous reports on planar CuSCN-based devices). For CBD deposited Sb_2S_3 devices with TiO_2 as the ETL, the performance is at par with the PCE reported by Wang *et al.*[31] (2.0%) and Lei *et al.* (1.9%)[32] using organic spiro-OMeTAD and P3HT as the HTLs, respectively. The relatively low FFs of both these cells are also a result of the incomplete coverage of the TiO_2 surface with the Sb_2S_3 ultrathin film (*ca.* $\sim$40–50 nm in Fig. 2c), which would induce a shunt path between the electron and hole transport layers (supported by shunted devices obtained with devices without the CuSCN layer, shown in Fig. S1c and Table S3, ESI†).
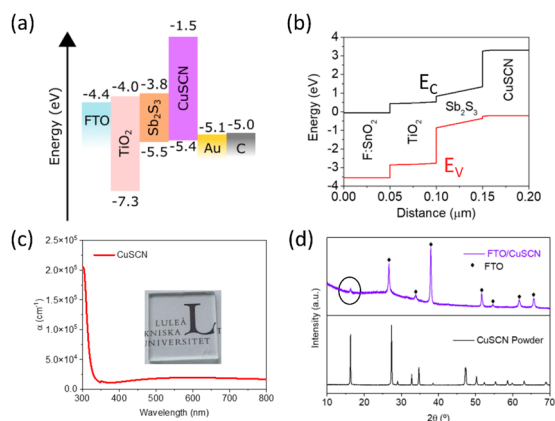

Fig. 1 (a) The energy level diagram of each layer in the FTO/TiO_2/Sb_2S_3/CuSCN/Au (or carbon) solar cells. (b) SCAPS-1D modeling determined energy band diagram of the solar cells at short circuit. (c) The absorption coefficient of a CuSCN thin film on a glass substrate. (d) X-Ray diffraction pattern of commercial CuSCN powder and the prepared CuSCN film on the FTO substrate.
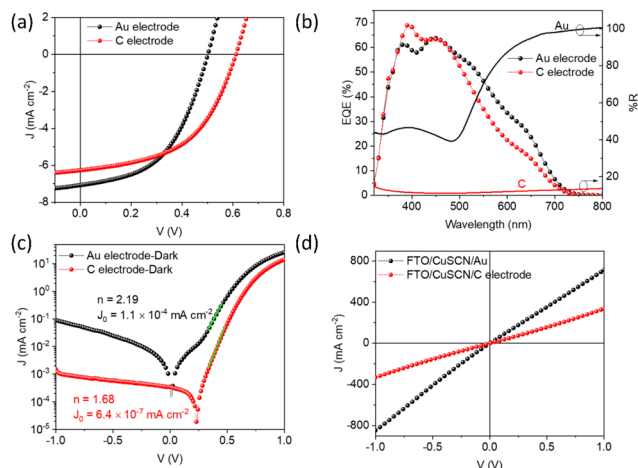
16276 | *J. Mater. Chem. C*, 2022, **10**, 16273–16282

This journal is © The Royal Society of Chemistry 2022

Fig. 3 (a) Light J–V curves and (b) external quantum efficiency of champion solar cells with Au and C electrodes, along with the reflectance spectrum of Au and C electrodes. (c) Corresponding dark J–V curves, used for the calculation of the device ideality factor (n) and reverse saturation current density (J_0). (d) Linear J–V curve for FTO/CuSCN/electrode devices.

Even with this highly porous active layer, little hysteresis was seen in the forward *vs.* reverse scan in the control device with the Au electrode, suggesting efficient charge transfer at the Sb_2S_3/HTL interface (Fig. S7, ESI†).

Increasing the thickness of the Sb_2S_3 layer did not increase the J_{SC}, and the performance was limited by all the parameters being low: lower J_{SC}, V_{OC}, and FF (see Fig. S1a and Table S1, ESI†). This observation agrees with the report by Zhang *et al.*[75] In a previous report by Christians *et al.*,[76] a similar planar device structure (FTO/TiO$_2$/CBD-Sb$_2$S$_3$/CuSCN/Au) was studied to estimate the maximum Sb_2S_3 thickness of ∼50 nm to balance light absorption and charge extraction. Furthermore, in CBD deposited Sb_2S_3, impurity phases like Sb_2O_3 and $Sb_2(SO_3)_3$ are inevitable since the reaction takes place in water.[19,75] Since oxide impurities were not discernible from the XRD spectrum of a thin film of ∼90 nm (Fig. S3d, ESI†), a highly sensitive RBS measurement was carried out to analyze the composition of the CBD deposited Sb_2S_3 films (Fig. S8, ESI†). An optically active film has been deposited on the Si substrate for RBS analysis to avoid interference of heavy elements from FTO. The SbS film presents a homogeneous in-depth composition, with the presence of a significant amount of oxygen. The atomic composition of the film is $Sb_{2.0}S_{2.1}O_{1.3}$, with a 24% atomic content of oxygen. Lian *et al.* used deep-level transient spectroscopy to study the defects in Sb_2S_3 with variations in composition.[77] At smaller concentrations, oxygen impurities can passivate defects caused by S deficit, while excessive oxygen (like in the current analysis) would form detrimental O_{Sb} defects. Cai *et al.*[78] used first-principles calculations to show that O can easily replace S in Sb_2S_3 (O_S), leading to poor conductivity and a high hole-trap concentration. Surface treatments with a sulfur source have been suggested by Choi *et al.*[23] to reduce the oxide phases, leading to as high as 29% improvement in photovoltaic performance. Hence, optimization of the active layer could be the

focus of future studies focusing mainly on PCE improvements with the current device structure.

The short circuit current density, J_{SC}, is influenced by the absorption and charge extraction properties of the solar cells. Comparatively, the lower J_{SC} of the C-electrode device can be reasoned using the external quantum efficiency (EQE) and reflectance spectrum of electrodes (Fig. 3b). The integrated J_{SC} values were in close agreement with the J–V curves (7.7 and 6.6 mA cm^{-2}, for C and Au electrodes, respectively). The reflectance contribution in the EQE curve from the back electrode in the wavelength range of 600–700 nm is significantly higher for Au-solar cells (the internal quantum efficiency curve in Fig. S9 (ESI†) clearly shows that enhancement in the longer wavelength region). This observation has been reported elsewhere, using carbon electrodes.[53] The carbon electrode reflects barely any light (<5% reflectance for all wavelengths in Fig. 3b). At the same time, an ultrathin Sb_2S_3 absorber layer cannot absorb all the light, especially the longer wavelengths (as can be seen in Fig. S3a (ESI†), the absorption coefficient of Sb_2S_3 drops steeply in the longer wavelength region). The Au electrode can reflect the unabsorbed transmitted light and contribute to higher EQE in the longer wavelength region and, hence, higher J_{SC}. At the lower wavelength region where the reflectance from the Au electrode decreases sharply, lower EQE for Au electrode suggests that the photocurrent is dominated by drift current under the influence of a built-in electric field and charge extraction efficiency of the electrodes.[79] The carbon electrode, thus, could collect holes more efficiently as the electron contacts are the same for both the devices. This is confirmed from the recombination resistance (R_{rec}) and built-in potential (V_{bi}) values calculated for the two devices in the subsequent analysis of the device.

Series and shunt resistances of the two devices in light were calculated from the linear region slopes near open circuit (R_s = dJ/$dV|_{V=V_{OC}}$) and short circuit (R_{sh} = dJ/$dV|_{V=0V}$) conditions, respectively.[80] The series resistance of the Au-device was slightly lower (8.15 Ω cm^{-2} for the Au-device *vs.* 8.6 Ω cm^{-2} for the C-device, calculated in the linear region near V_{OC}). However, the shunt resistance for the Au device is much lower (505 Ω cm^{-2}) compared to that of the C-device (636 Ω cm^{-2}). A higher shunt resistance in the C-device means enhanced recombination resistance and higher FF and V_{OC}.

Moreover, theoretically, V_{OC} should be independent of the electrode since it depends on the quasi-Fermi level energy splitting between the ETL and the HTL in n-i-p solar cells.[81–83] Also, given that the WF of C and Au is similar (−5.0 and −5.1 eV, respectively),[53] the V_{OC} values are expected to be similar.[84] The reason for increased V_{OC} (statistics of variation in performance parameters among devices is shown in Fig. S6, ESI†) of the C-electrode solar cell was studied in detail since it is the major limitation in $Sb_2(S,Se)_3$ solar cells.[85] V_{oc} depends on the diode ideality factor, n, and saturation current density, J_0 as:

$$V_{oc} = \frac{nkT}{q} \ln\left(\frac{J_{SC}}{J_0} + 1\right)$$

This journal is © The Royal Society of Chemistry 2022

J. Mater. Chem. C, 2022, **10**, 16273–16282 | **16277**

where n represents the diode ideality factor, k is the Boltzmann constant, T is the absolute temperature, and q is the elementary charge.[86] J_0 and n values are calculated from the dark J–V characteristics (the fitting region is shown in Fig. 3c) using the Shockley diode equation:[87]

$$J = J_0\left(\exp\left(\frac{qV}{nkT}\right) - 1\right)$$

The ideality factor of the C-electrode solar cell ($n = 1.68$) is lower than that of the Au-electrode solar cell ($n = 2.19$). Since the HTL and ETL are the same for the devices and V_{OC} was significantly different, the ideality factor values represent both bulk recombination and surface recombination at the contacts.[88] J_0 decreased by almost three orders of magnitude from 1.1×10^{-4} to 6.4×10^{-7} mA cm^{-2} using a C electrode $vs.$ Au electrode. Both these values suggest reduced recombination (contact interface and bulk) and thus higher V_{OC} and FF for C-based devices.[89] Higher leakage currents also suggest a comparatively higher shunting in the Au device (the rectification ratio of dark currents at ±1 V was $ca.$ 14 350 for C electrode and 287 for Au electrode). This shunting behavior complicates the direct comparison between these devices based only on dark IV analysis.[90]

It is also noteworthy that both electrodes form a near-Ohmic contact with the CuSCN layer (Fig. 3d). Therefore, the V_{OC} discrepancy does not seem to originate from energy level offsets (leading to an injection barrier) between the electrode and HTL.[83] It is likely that the physical contact between carbon and CuSCN is more passivating in nature as compared to the Au electrode, indicating less surface recombination at contacts. Notably, the CuSCN surface did not show a visible change with the solvent used in the C paste because of the limited solubility of CuSCN in common solvents such as xylene (Fig. S5a–c, ESI†).[91]

Furthermore, interface and charge transport characteristics of the cells with Au and C/Ag back-contact were studied using electrochemical impedance spectroscopy measurements (EIS) in the dark at an applied voltage of 0.5 V (close to V_{OC}). The Nyquist plot showed a single depressed semicircle which is modeled by a series resistance component, $R_{S,EIS}$ (combining all resistances including that of electrodes) in series with a parallel combination of recombination resistance (R_{rec})—constant phase element (CPE). The $R_{S,EIS}$ value for Au-device is slightly lower because of the reduced resistance of the Au electrode, while the R_{rec} for C-device is substantially higher (Table S6, ESI†). High R_{rec} implies reduced recombination in the C-device, thus higher V_{OC}. Since the TiO$_2$/Sb$_2$S$_3$ and Sb$_2$S$_3$/CuSCN interfaces are identical and WFs of electrodes are similar in both cases, the R_{rec} values are primarily associated with the CuSCN/electrode interfaces. This observation is consistent with the reports where C-electrode has been reported to possess both HTL and charge collection properties.[92–94]

Capacitance–voltage (C–V) measurements were carried out to study the carrier accumulation and transport properties at the interface.[95,96] Capacitance response in these measurements
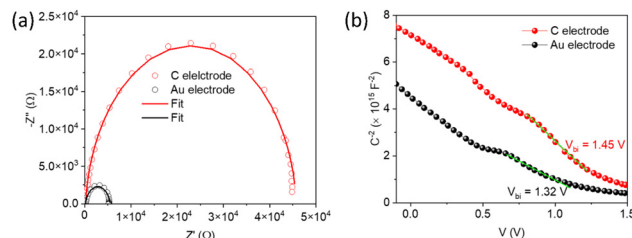

Fig. 4 Nyquist plots (a) and Mott–Schottky with fitted line plots (b) for C and Au-based solar cell devices.

corresponds to free carriers along with bulk and interfacial defects.[97] For the devices studied here, the differences in the capacitance response would arise from different charge extraction properties of the contacts. Fig. 4b shows Mott–Schottky (M–S) plots of devices with the two electrodes at 10 kHz in the dark. It shows a bias-dependent capacitance demonstrating the presence of an abrupt p–n$^+$ (Sb$_2$S$_3$/TiO$_2$) junction, where TiO$_2$ is a highly doped n-type material (calculated $N_D = 2.4 \times 10^{19}$ cm^{-3}, and the corresponding Mott–Schottky analysis shown in Fig. S10, ESI†).[98,99] The charge carrier (acceptor) concentration (N_A) at the edge of the p-side depletion region and total build-in potential (V_{bi}) were calculated using the following equation:

$$\frac{1}{C^2} = \frac{2\left(\varepsilon_{Sb_2S_3}N_A + \varepsilon_{TiO_2}N_D\right)(V_{bi} - V)}{qA^2\varepsilon_o\varepsilon_{Sb_2S_3}N_A\varepsilon_{TiO_2}N_D}$$

where ε_0, $\varepsilon_{Sb_2S_3/TiO_2}$, and A represent vacuum permittivity, dielectric constant of Sb$_2$S$_3$ ($\varepsilon_{Sb_2S_3} = 7.1$)/TiO$_2$ ($\varepsilon_{TiO_2} = 51$), and device active area, respectively.[100–102] The linear fitting slope in the C^{-2} $vs.$ voltage curve at a positive voltage was used to calculate the N_A and the extrapolation to the voltage axis was used to extract the V_{bi} (the fitting line is shown in Fig. 4b). The device with a C-electrode shows a higher V_{bi} of 1.45 V and a carrier density (N_A) of 9.5×10^{16} cm^{-3} compared with those of the Au-electrode (1.32 V and 1.8×10^{17} cm^{-3}, respectively). The higher built-in potential relates to increased V_{OC}, less carrier accumulation, and efficient hole extraction at the HTL/electrode interface.[95] Finally, Capacitance–frequency (C–f) plots to identify the defect type at 0 V bias of both the devices are shown in Fig. S11 (ESI†). The increased capacitance of the Au-device in the low-frequency regime and increased frequency dependence can be attributed to charge accumulation at the contact interface.[96] The screening effect of this charge accumulation increases the recombination loss, decreases the V_{bi}, and thus reduces the V_{OC}.[89,96,103,104]

Since the electron transport and collection side are the same for both devices, the calculated parameters mentioned above point to an inefficient charge collection and possible shunt at the CuSCN/Au interface. The blade-coated carbon electrode with large graphite flakes (Fig. S4, ESI†) is less prone to shunting than the vacuum deposited Au electrode and makes intimate contact with the CuSCN layer. This is supported by the peel-off test using a strong copper adhesive tape. The Au electrode was peeled off while the carbon electrode remained
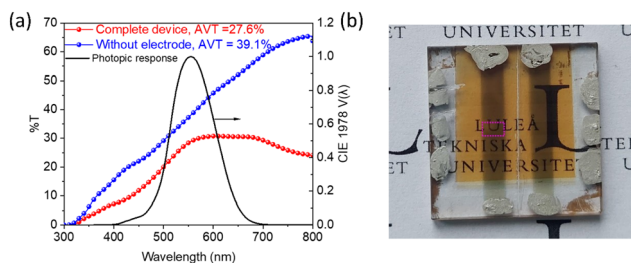
Fig. 5 (a) Transmission spectrum of the semitransparent device with and without a top electrode ($\sim$15 nm Au), along with the human eye's photopic response. (b) Photograph of a semitransparent device with the active area marked using a pink dotted rectangle.

intact, suggesting intimate contact with the underlying CuSCN layer (Fig. S12, ESI†). A similar observation has been reported by Aung et al.[105]

The high transparency of CuSCN thin films (with a wide bandgap of 3.85 eV) and an extremely thin Sb_2S_3 absorber layer enable a semitransparent solar cell. A high AVT of $\sim$27.5% for the complete device (for the device without top electrode AVT = 39.1% vs. air was calculated) and a PCE of 1.67% (V_{OC} = 0.560 V, J_{SC} = 6.12 mA cm^{-2}, and FF = 0.49) were obtained with the same structure as that of opaque Au electrode-based solar cells, except that the electrode thickness was reduced to $\sim$15 nm (Fig. 5a and b). Further optimization is needed to achieve the highest light utilization efficiency (LUE = PCE $\times$ AVT) since PCE and AVT are mostly inversely related. For example, a solution-processed carbon-based transparent top electrode such as graphene could replace the vacuum-processed ultrathin Au electrode.[106] However, this report focuses on the viability of a semitransparent Sb_2S_3 solar cell using this combination of inorganic electron (TiO_2) and hole (CuSCN) transport layers. Further optimization of the absorber layer composition and morphology would be carried out using different deposition methods and post-deposition treatments to reduce the amount of oxygen impurities,[23] obtain larger grains,[107] and achieve preferential [hk1] orientation[17,108–111] of Sb_2S_3 crystallites (compared to predominantly [hk0] in the obtained thin film shown in Fig. S3d, ESI†). Also, a stability study in comparison to the organic HTL layer would be carried out to illustrate the inherent stability of the device layer vs. the stability of the completed device.

Conclusions

In summary, a compact CuSCN layer deposited via spin coating under ambient conditions suppressed the shunt paths in the chemical bath deposited Sb_2S_3 solar cells implementing a simple planar configuration—FTO/TiO_2/Sb_2S_3/CuSCN/Au or C/Ag. The robust CuSCN layer showed good interfacial contact with the carbon electrode resulting in even improved solar cell performance compared to the vacuum-deposited Au electrode, achieving a PCE of 1.95%. A higher V_{OC} in carbon-based devices is attributed to better diode characteristics, high recombination resistance, and a higher V_{bi}. Enhancing V_{OC} using an improved

CuSCN/electrode interface is a promising direction for future studies since a significant limitation in the performance of Sb_2S_3 solar cells stems from voltage loss ($>$50% lower than the SQ limit of 1.4 V).[85] Moreover, the high transparency and smoothness of the CuSCN layer allowed achieving a preliminary semitransparent solar device with an impressive AVT of 26.7% with a PCE of 1.67%. The lower overall PCE, though, is reflective of a low-quality CBD deposited absorber layer with high amounts of oxygen impurities and unfavorable (hk0) orientation, which can be overcome by alternate deposition methods like rapid thermal evaporation, vapor transport deposition, ALD, and so on.[11] Overall, the focus of this study was to demonstrate the compatibility and potential of CuSCN as the HTL in Sb_2S_3 (or potentially in Sb_2Se_3 because of a similar crystal structure) solar cell devices using carbon electrodes and semitransparent solar cell devices.

Author contributions

Conflicts of interest

There are no conflicts to declare.

Acknowledgements

References

1 O. Almora, D. Baran, G. C. Bazan, C. Berger, C. I. Cabrera, K. R. Catchpole, S. Erten-Ela, F. Guo, J. Hauch, A. W. Y. Ho-Baillie, T. J. Jacobsson, R. A. J. Janssen, T. Kirchartz, N. Kopidakis, Y. Li, M. A. Loi, R. R. Lunt, X. Mathew, M. D. McGehee, J. Min, D. B. Mitzi, M. K. Nazeeruddin, J. Nelson, A. F. Nogueira, U. W. Paetzold, N.-G. Park, B. P. Rand, U. Rau, H. J. Snaith, E. Unger, L. Vaillant-Roca, H.-L. Yip and C. J. Brabec, Adv. Energy Mater., 2021, 11, 2102526.

2 A. Zakutayev, J. D. Major, X. Hao, A. Walsh, J. Tang, T. K. Todorov, L. H. Wong and E. Saucedo, J. Phys. Energy, 2021, 3, 032003.

3 Y. Sun, H. Xu, Y. Kan and K. Gao, Sci. China Mater., 2022, 65, 2609–2610.

4 Y. Sun, R. Ma, Y. Kan, T. Liu, K. Zhou, P. Liu, J. Fang, Y. Chen, L. Ye, C. Ma, H. Yan and K. Gao, Macromol. Rapid Commun., 2022, 2200139.

5 R. Ma, K. Zhou, Y. Sun, T. Liu, Y. Kan, Y. Xiao, T. A. Dela Peña, Y. Li, X. Zou, Z. Xing, Z. Luo, K. S. Wong, X. Lu, L. Ye, H. Yan and K. Gao, Matter, 2022, 5, 725–734.

This journal is © The Royal Society of Chemistry 2022

J. Mater. Chem. C, 2022, 10, 16273–16282 | 16279

6 M. He, C. Yan, J. Li, M. P. Suryawanshi, J. Kim, M. A. Green and X. Hao, *Adv. Sci.*, 2021, **8**, 2004313.

7 O. Almora, D. Baran, G. C. Bazan, C. Berger, C. I. Cabrera, K. R. Catchpole, S. Erten-Ela, F. Guo, J. Hauch, A. W. Y. Ho-Baillie, T. J. Jacobsson, R. A. J. Janssen, T. Kirchartz, N. Kopidakis, Y. Li, M. A. Loi, R. R. Lunt, X. Mathew, M. D. McGehee, J. Min, D. B. Mitzi, M. K. Nazeeruddin, J. Nelson, A. F. Nogueira, U. W. Paetzold, N.-G. Park, B. P. Rand, U. Rau, H. J. Snaith, E. Unger, L. Vaillant-Roca, H.-L. Yip and C. J. Brabec, *Adv. Energy Mater.*, 2021, **11**, 2002774.

8 L. H. Wong, A. Zakutayev, J. D. Major, X. Hao, A. Walsh, T. K. Todorov and E. Saucedo, *J. Phys. Energy*, 2019, **1**, 032001.

9 R. Nie, M. Hu, A. M. Risqi, Z. Li and S. I. Seok, *Adv. Sci.*, 2021, **8**, 2003172.

10 S. Rühle, *Sol. Energy*, 2016, **130**, 139–147.

11 Q. Wang, Z. Chen, J. Wang, Y. Xu, Y. Wei, Y. Wei, L. Qiu, H. Lu, Y. Ding and J. Zhu, *Inorg. Chem. Front.*, 2019, **6**, 3381–3397.

12 M. Y. Versavel and J. A. Haber, *Thin Solid Films*, 2007, **515**, 7171–7176.

13 X. Wang, Z. Li, S. R. Kavanagh, A. M. Ganose and A. Walsh, *Phys. Chem. Chem. Phys.*, 2022, **24**, 7195–7202.

14 H. Deng, Y. Zeng, M. Ishaq, S. Yuan, H. Zhang, X. Yang, M. Hou, U. Farooq, J. Huang, K. Sun, R. Webster, H. Wu, Z. Chen, F. Yi, H. Song, X. Hao and J. Tang, *Adv. Funct. Mater.*, 2019, **29**, 1901720.

15 Z. Yang, X. Wang, Y. Chen, Z. Zheng, Z. Chen, W. Xu, W. Liu, Y. (Michael) Yang, J. Zhao, T. Chen and H. Zhu, *Nat. Commun.*, 2019, **10**, 4540.

16 R. Kondrotas, C. Chen and J. Tang, *Joule*, 2018, **2**, 857–878.

17 X. Jin, Y. Fang, T. Salim, M. Feng, S. Hadke, S. W. Leow, T. C. Sum and L. H. Wong, *Adv. Funct. Mater.*, 2020, **30**, 2002887.

18 U. A. Shah, S. Chen, G. M. G. Khalaf, Z. Jin and H. Song, *Adv. Funct. Mater.*, 2021, **31**, 2100265.

19 A. Darga, D. Mencaraglia, C. Longeaud, T. J. Savenije, B. O'Regan, S. Bourdais, T. Muto, B. Delatouche and G. Dennler, *J. Phys. Chem. C*, 2013, **117**, 20525–20530.

20 R. Tang, X. Wang, C. Jiang, S. Li, W. Liu, H. Ju, S. Yang, C. Zhu and T. Chen, *ACS Appl. Mater. Interfaces*, 2018, **10**, 30314–30321.

21 P. P. Boix, Y. H. Lee, F. Fabregat-Santiago, S. H. Im, I. Mora-Sero, J. Bisquert and S. I. Seok, *ACS Nano*, 2012, **6**, 873–880.

22 J. Han, S. Wang, J. Yang, S. Guo, Q. Cao, H. Tang, X. Pu, B. Gao and X. Li, *ACS Appl. Mater. Interfaces*, 2020, **12**, 4970–4979.

23 Y. C. Choi, D. U. Lee, J. H. Noh, E. K. Kim and S. I. Seok, *Adv. Funct. Mater.*, 2014, **24**, 3587–3592.

24 S.-J. Lee, S.-J. Sung, K.-J. Yang, J.-K. Kang, J. Y. Kim, Y. S. Do and D.-H. Kim, *ACS Appl. Energy Mater.*, 2020, **3**, 12644–12651.

25 J. S. Eensalu, A. Katerski, E. Kärber, L. Weinhardt, M. Blum, C. Heske, W. Yang, I. Oja Acik and M. Krunks, *Beilstein J. Nanotechnol.*, 2019, **10**, 2396–2409.

26 L. Zhang, C. Jiang, C. Wu, H. Ju, G. Jiang, W. Liu, C. Zhu and T. Chen, *ACS Appl. Mater. Interfaces*, 2018, **10**, 27098–27105.

27 J. Zhang, W. Lian, Y. Yin, X. Wang, R. Tang, C. Qian, X. Hao, C. Zhu and T. Chen, *Sol. RRL*, 2020, **4**, 2000048.

28 E. Zimmermann, T. Pfadler, J. Kalb, J. A. Dorman, D. Sommer, G. Hahn, J. Weickert and L. Schmidt-Mende, *Adv. Sci.*, 2015, **2**, 1500059.

29 X. Wang, R. Tang, C. Wu, C. Zhu and T. Chen, *J. Energy Chem.*, 2018, **27**, 713–721.

30 T. Englman, E. Terkieltaub and L. Etgar, *J. Phys. Chem. C*, 2015, **119**, 12904–12909.

31 X. Wang, J. Li, W. Liu, S. Yang, C. Zhu and T. Chen, *Nanoscale*, 2017, **9**, 3386–3390.

32 H. Lei, G. Yang, Y. Guo, L. Xiong, P. Qin, X. Dai, X. Zheng, W. Ke, H. Tao, Z. Chen, B. Li and G. Fang, *Phys. Chem. Chem. Phys.*, 2016, **18**, 16436–16443.

33 Y. O. Mayon, T. P. White, R. Wang, Z. Yang and K. R. Catchpole, *Phys. Status Solidi A*, 2016, **213**, 108–113.

34 N. Wijeyasinghe, A. Regoutz, F. Eisner, T. Du, L. Tsetseris, Y.-H. Lin, H. Faber, P. Pattanasattayavong, J. Li, F. Yan, M. A. McLachlan, D. J. Payne, M. Heeney and T. D. Anthopoulos, *Adv. Funct. Mater.*, 2017, **27**, 1701818.

35 R. Singh, P. K. Singh, B. Bhattacharya and H.-W. Rhee, *Appl. Mater. Today*, 2019, **14**, 175–200.

36 K. Li, S. Wang, C. Chen, R. Kondrotas, M. Hu, S. Lu, C. Wang, W. Chen and J. Tang, *J. Mater. Chem. A*, 2019, **7**, 9665–9672.

37 H. Deng, S. Chen, M. Ishaq, Y. Cheng, Q. Sun, X. Lin, Q. Zheng, C. Zhang and S. Cheng, *Sol. RRL*, 2022, **6**, 2101017.

38 M. Ishaq, H. Deng, U. Farooq, H. Zhang, X. Yang, U. A. Shah and H. Song, *Sol. RRL*, 2019, **3**, 1900305.

39 Y. Itzhaik, O. Niitsoo, M. Page and G. Hodes, *J. Phys. Chem. C*, 2009, **113**, 4254–4256.

40 K. Tsujimoto, D.-C. Nguyen, S. Ito, H. Nishino, H. Matsuyoshi, A. Konno, G. R. A. Kumara and K. Tennakone, *J. Phys. Chem. C*, 2012, **116**, 13465–13471.

41 S. Ito, K. Tsujimoto, D.-C. Nguyen, K. Manabe and H. Nishino, *Int. J. Hydrogen Energy*, 2013, **38**, 16749–16754.

42 T. Muto, G. Larramona and G. Dennler, *Appl. Phys. Express*, 2013, **6**, 072301.

43 Y. Zhao, P. Cheng, H. Yang, M. Wang, D. Meng, Y. Zhu, R. Zheng, T. Li, A. Zhang, S. Tan, T. Huang, J. Bian, X. Zhan, P. S. Weiss and Y. Yang, *ACS Nano*, 2022, **16**, 1231–1238.

44 P. Cheng, H.-C. Wang, Y. Zhu, R. Zheng, T. Li, C.-H. Chen, T. Huang, Y. Zhao, R. Wang, D. Meng, Y. Li, C. Zhu, K-H. Wei, X. Zhan and Y. Yang, *Adv. Mater.*, 2020, **32**, 2003891.

45 Y. Liu, P. Cheng, T. Li, R. Wang, Y. Li, S.-Y. Chang, Y. Zhu, H.-W. Cheng, K-H. Wei, X. Zhan, B. Sun and Y. Yang, *ACS Nano*, 2019, **13**, 1071–1077.

46 J. Sun and J. J. Jasieniak, *J. Phys. Appl. Phys.*, 2017, **50**, 093001.

47 A. A. F. Husain, W. Z. W. Hasan, S. Shafie, M. N. Hamidon and S. S. Pandey, *Renewable Sustainable Energy Rev.*, 2018, **94**, 779–791.

16280 | *J. Mater. Chem. C*, 2022, **10**, 16273–16282

This journal is © The Royal Society of Chemistry 2022

48 M. Saifullah, J. Gwak and J. H. Yun, *J. Mater. Chem. A*, 2016, **4**, 8512–8540.

49 Z. Chen and G. Chen, *Sol. Energy*, 2020, **201**, 323–329.

50 R. Tang, X. Wang, W. Lian, J. Huang, Q. Wei, M. Huang, Y. Yin, C. Jiang, S. Yang, G. Xing, S. Chen, C. Zhu, X. Hao, M. A. Green and T. Chen, *Nat. Energy*, 2020, **5**, 587–595.

51 J. Han, X. Pu, H. Zhou, Q. Cao, S. Wang, Z. He, B. Gao, T. Li, J. Zhao and X. Li, *ACS Appl. Mater. Interfaces*, 2020, **12**, 44297–44306.

52 C. Jiang, R. Tang, X. Wang, H. Ju, G. Chen and T. Chen, *Sol. RRL*, 2019, **3**, 1800272.

53 G. A. Sepalage, H. Weerasinghe, N. Rai, N. W. Duffy, S. R. Raga, Y. Hora, M. Gao, D. Vak, A. S. R. Chesman, U. Bach and A. N. Simonov, *Adv. Mater. Technol.*, 2022, **7**, 2101148.

54 N. Wijeyasinghe, F. Eisner, L. Tsetseris, Y.-H. Lin, A. Seitkhan, J. Li, F. Yan, O. Solomeshch, N. Tessler, P. Patsalas and T. D. Anthopoulos, *Adv. Funct. Mater.*, 2018, **28**, 1802055.

55 J. Peng, F. Kremer, D. Walter, Y. Wu, Y. Ji, J. Xiang, W. Liu, T. Duong, H. Shen, T. Lu, F. Brink, D. Zhong, L. Li, O. Lee Cheong Lem, Y. Liu, K. J. Weber, T. P. White and K. R. Catchpole, *Nature*, 2022, **601**, 573–578.

56 S. Messina, M. T. S. Nair and P. K. Nair, *Thin Solid Films*, 2007, **515**, 5777–5782.

57 J. W. Jung, C.-C. Chueh and A. K.-Y. Jen, *Adv. Energy Mater.*, 2015, **5**, 1500486.

58 C. Chen, W. Li, Y. Zhou, C. Chen, M. Luo, X. Liu, K. Zeng, B. Yang, C. Zhang, J. Han and J. Tang, *Appl. Phys. Lett.*, 2015, **107**, 043905.

59 Y. Li, W. Yan, Y. Li, S. Wang, W. Wang, Z. Bian, L. Xiao and Q. Gong, *Sci. Rep.*, 2015, **5**, 14485.

60 E. Cárdenas, A. Arato, E. Perez-Tijerina, T. K. Das Roy, G. Alan Castillo and B. Krishnan, *Sol. Energy Mater. Sol. Cells*, 2009, **93**, 33–36.

61 L. Guo, B. Zhang, S. Li, Q. Zhang, M. Buettner, L. Li, X. Qian and F. Yan, *APL Mater.*, 2019, **7**, 041105.

62 X.-D. Gao, X.-M. Li, W.-D. Yu, J.-J. Qiu and X.-Y. Gan, *Thin Solid Films*, 2008, **517**, 554–559.

63 B. R. Sankapal, E. Goncalves, A. Ennaoui and M. C. Lux-Steiner, *Thin Solid Films*, 2004, **451–452**, 128–132.

64 K. Lee, H.-D. Um, D. Choi, J. Park, N. Kim, H. Kim and K. Seo, *Cell Rep. Phys. Sci.*, 2020, **1**, 100143.

65 A. S. Bondarenko and G. A. Ragoisha, *Nova Sci.*, New York, https//www.abc.chemistry.bsu.by/vi/, 2005, 1110–1112.

66 M. Burgelman, P. Nollet and S. Degrave, *Thin Solid Films*, 2000, **361–362**, 527–532.

67 I. S. Yang, M. R. Sohn, S. D. Sung, Y. J. Kim, Y. J. Yoo, J. Kim and W. I. Lee, *Nano Energy*, 2017, **32**, 414–421.

68 S. Ito, S. Tanaka and H. Nishino, *J. Phys. Chem. Lett.*, 2015, **6**, 881–886.

69 S. Chavhan, O. Miguel, H.-J. Grande, V. Gonzalez-Pedro, R. S. Sánchez, E. M. Barea, I. Mora-Seró and R. Tena-Zaera, *J. Mater. Chem. A*, 2014, **2**, 12754–12760.

70 L. Fan, Y. Li, X. Yao, Y. Ding, S. Zhao, B. Shi, C. Wei, D. Zhang, B. Li, G. Wang, Y. Zhao and X. Zhang, *ACS Appl. Energy Mater.*, 2018, **1**, 1575–1584.

71 A. Montgomery, L. Guo, C. Grice, R. A. Awni, S. Saurav, L. Li, Y. Yan and F. Yan, *Prog. Photovolt.: Res. Appl.*, 2019, **27**, 665–672.

72 M. Jung, Y. C. Kim, N. J. Jeon, W. S. Yang, J. Seo, J. H. Noh and S. Il Seok, *ChemSusChem*, 2016, **9**, 2592–2596.

73 S. Ye, W. Sun, Y. Li, W. Yan, H. Peng, Z. Bian, Z. Liu and C. Huang, *Nano Lett.*, 2015, **15**, 3723–3728.

74 N. Arora, M. I. Dar, A. Hinderhofer, N. Pellet, F. Schreiber, S. M. Zakeeruddin and M. Grätzel, *Science*, 2017, **358**, 768–771.

75 X. Zhang, S. Yoshioka, N. Loew and M. Ihara, *ECS Trans.*, 2014, **64**, 1.

76 J. A. Christians, D. T. Leighton and P. V. Kamat, *Energy Environ. Sci.*, 2014, **7**, 1148–1158.

77 W. Lian, C. Jiang, Y. Yin, R. Tang, G. Li, L. Zhang, B. Che and T. Chen, *Nat. Commun.*, 2021, **12**, 3260.

78 Z. Cai, C.-M. Dai and S. Chen, *Sol. RRL*, 2020, **4**, 1900503.

79 M.-J. Choi, S. Kim, H. Lim, J. Choi, D. M. Sim, S. Yim, B. T. Ahn, J. Y. Kim and Y. S. Jung, *Adv. Mater.*, 2016, **28**, 1780–1787.

80 D. S. H. Chan and J. C. H. Phang, *IEEE Trans. Electron Devices*, 1987, **34**, 286–293.

81 K. Shen, Y. Zhang, X. Wang, C. Ou, F. Guo, H. Zhu, C. Liu, Y. Gao, R. E. I. Schropp, Z. Li, X. Liu and Y. Mai, *Adv. Sci.*, 2020, **7**, 2001013.

82 C. Chen, L. Wang, L. Gao, D. Nam, D. Li, K. Li, Y. Zhao, C. Ge, H. Cheong, H. Liu, H. Song and J. Tang, *ACS Energy Lett.*, 2017, **2**, 2125–2132.

83 P. R. Brown, R. R. Lunt, N. Zhao, T. P. Osedach, D. D. Wanger, L.-Y. Chang, M. G. Bawendi and V. Bulović, *Nano Lett.*, 2011, **11**, 2955–2961.

84 P. Mariani, L. Najafi, G. Bianca, M. I. Zappia, L. Gabatel, A. Agresti, S. Pescetelli, A. Di Carlo, S. Bellani and F. Bonaccorso, *ACS Appl. Mater. Interfaces*, 2021, **13**, 22368–22380.

85 J. Dong, Y. Liu, Z. Wang and Y. Zhang, *Nano Sel.*, 2021, **2**, 1818–1848.

86 V. Nadenau, U. Rau, A. Jasenek and H. W. Schock, *J. Appl. Phys.*, 2000, **87**, 584–593.

87 J. R. Sites and P. H. Mauk, *Sol. Cells*, 1989, **27**, 411–417.

88 O. J. Sandberg, A. Sundqvist, M. Nyman and R. Österbacka, *Phys. Rev. Appl.*, 2016, **5**, 044005.

89 S. Yuan, H. Deng, X. Yang, C. Hu, J. Khan, W. Ye, J. Tang and H. Song, *ACS Photonics*, 2017, **4**, 2862–2870.

90 T. Kirchartz, F. Deledalle, P. S. Tuladhar, J. R. Durrant and J. Nelson, *J. Phys. Chem. Lett.*, 2013, **4**, 2371–2376.

91 N. Chaudhary, R. Chaudhary, J. P. Kesari and A. Patra, *Opt. Mater.*, 2017, **69**, 367–371.

92 W. Chen, L. Jiang, R. Pathak and F. Wu, *ECS J. Solid State Sci. Technol.*, 2019, **8**, Q67.

93 E. Calabrò, F. Matteocci, B. Paci, L. Cinà, L. Vesce, J. Barichello, A. Generosi, A. Reale and A. Di Carlo, *ACS Appl. Mater. Interfaces*, 2020, **12**, 32536–32547.

94 H. Zhou, Y. Shi, Q. Dong, H. Zhang, Y. Xing, K. Wang, Y. Du and T. Ma, *J. Phys. Chem. Lett.*, 2014, **5**, 3241–3246.

This journal is © The Royal Society of Chemistry 2022

J. Mater. Chem. C, 2022, **10**, 16273–16282 | **16281**

95 U. K. Thakur, P. Kumar, S. Gusarov, A. E. Kobryn, S. Riddell, A. Goswami, K. M. Alam, S. Savela, P. Kar, T. Thundat, A. Meldrum and K. Shankar, *ACS Appl. Mater. Interfaces*, 2020, **12**, 11467–11478.

96 E. von Hauff, *J. Phys. Chem. C*, 2019, **123**, 11329–11346.

97 W. Wang, X. Wang, G. Chen, L. Yao, X. Huang, T. Chen, C. Zhu, S. Chen, Z. Huang and Y. Zhang, *Adv. Electron. Mater.*, 2019, **5**, 1800683.

98 S. M. Willis, C. Cheng, H. E. Assender and A. A. R. Watt, *Nano Lett.*, 2012, **12**, 1522–1526.

99 A. Mani, C. Huisman, A. Goossens and J. Schoonman, *J. Phys. Chem. B*, 2008, **112**, 10086–10091.

100 M. T. Islam and A. K. Thakur, *Sol. Energy*, 2020, **202**, 304–315.

101 L. Kavan, N. Tétreault, T. Moehl and M. Grätzel, *J. Phys. Chem. C*, 2014, **118**, 16408–16418.

102 D. A. Neamen, *Semiconductor physics and devices: basic principles*, McGraw-Hill; New York, NY, 4th edn, 2012.

103 M. Burgelman and P. Nollet, *Solid State Ionics*, 2005, **176**, 2171–2175.

104 O. Almora, I. Zarazua, E. Mas-Marza, I. Mora-Sero, J. Bisquert and G. Garcia-Belmonte, *J. Phys. Chem. Lett.*, 2015, **6**, 1645–1652.

105 S. K. K. Aung, A. Vijayan, T. Seetawan and G. Boschloo, *Sol. RRL*, 2022, **6**, 2100773.

106 Y. Sun, T. Liu, Y. Kan, K. Gao, B. Tang and Y. Li, *Small Sci.*, 2021, **1**, 2100001.

107 U. Chalapathi, B. Poornaprakash, C.-H. Ahn and S.-H. Park, *Mater. Sci. Semicond. Process.*, 2018, **84**, 138–143.

108 Y. Zeng, K. Sun, J. Huang, M. P. Nielsen, F. Ji, C. Sha, S. Yuan, X. Zhang, C. Yan, X. Liu, H. Deng, Y. Lai, J. Seidel, N. Ekins-Daukes, F. Liu, H. Song, M. Green and X. Hao, *ACS Appl. Mater. Interfaces*, 2020, **12**, 22825–22834.

109 L. Liu, S.-L. Zhang, J.-Y. Wu, W.-H. Wang, W. Liu, L. Wu and Y. Zhang, *Chin. Phys. B*, 2020, **29**, 058801.

110 F. Li, C. Wang, P. Liu, Y. Xiao, L. Bai, F. Qi, X. Hou, H. Zhang, Y. Wang, S. Wang and X.-Z. Zhao, *Sol. RRL*, 2019, **3**, 1800297.

111 J. Chen, J. Qi, R. Liu, X. Zhu, Z. Wan, Q. Zhao, S. Tao, C. Dong, G. Y. Ashebir, W. Chen, R. Peng, F. Zhang, S. Yang, X. Tian and M. Wang, *Commun. Chem.*, 2019, **2**, 1–9.

16282 | *J. Mater. Chem. C*, 2022, **10**, 16273–16282

This journal is © The Royal Society of Chemistry 2022